

Scaling properties of the elastic stiffness moduli of a random rigid-nonrigid network near the rigidity threshold: Theory and simulations

Edgardo Duering

School of Physics and Astronomy, Raymond and Beverly Sackler Faculty of Exact Sciences, Tel Aviv University, 69 978 Tel Aviv, Israel

David J. Bergman

School of Physics and Astronomy, Raymond and Beverly Sackler Faculty of Exact Sciences, Tel Aviv University, 69 978 Tel Aviv, Israel and Department of Physics, The Ohio State University, Columbus, Ohio 43210-1106*

(Received 11 December 1987)

The critical properties of the elastic stiffness moduli of random rigid-nonrigid networks near the rigidity threshold p_c are investigated by constructing a scaling theory in terms of two scaling parameters. The theory is tested by simulations of a series of two-dimensional long-strip, two-component random networks at p_c , in which both components have finite bond-stretching and angle-bending force constants. The simulations also serve to determine the precise form of the scaling variables. Some new physical properties have emerged that will need to be understood theoretically and tested experimentally.

I. INTRODUCTION

The macroscopic elastic properties of random networks near a percolation threshold have received considerable attention in recent years.¹⁻¹⁴ Among the surprises that were uncovered was the phenomenon of a negative Poisson's ratio Σ . This was found to occur in mixtures of rigid and nonrigid bonds when the fraction of rigid bonds p is so close to the percolation threshold p_c that the correlation length ξ is much greater than the system (linear) size L .¹³ The negative value of Σ in that regime was found to be independent of the elementary or microscopic force constants of the bonds. These could therefore be chosen to mimic a material with a normal positive value for Σ . Thus a mechanism was discovered for constructing isotropic elastic materials with negative or zero Σ by mixing a normal elastic material with positive Σ and a rigid elastic material with infinite stiffness moduli. Since naturally occurring isotropic elastic materials always have a positive Σ , implementation of this mechanism could lead to a new class of synthetic elastic materials. Further work on such rigid-nonrigid mixed networks showed that the Poisson's ratio is sensitive to the precise value of ξ/L ,¹⁴ changing from about -0.3 when $\xi/L = \infty$ to about $+0.08$ when $\xi/L = 0$. A zero Poisson's ratio is obtained for $\xi/L \simeq 5$.

In this paper we describe results of theoretical and numerical work whose aim was to investigate the stiffness moduli and especially Poisson's ratio Σ in such a mixture when the rigid component has large but not infinite elastic moduli.

The microscopic model we used for the elastic properties of a two-dimensional (2D) random material has enough parameters in it (e.g., there are four different force constants) so that a number of different regimes can be accessed. In order to analyze the critical behavior

near the rigidity threshold in some detail, we have resorted to a scaling description. Scaling assumptions were made by drawing on results of previous calculations^{12,13} and also on what we know from the thoroughly studied critical behavior of random conducting networks near a conductivity threshold. These assumptions were then tested by comparing them with the results of a series of simulations of 2D random elastic networks.

The rest of this paper is organized as follows: In Sec. II we develop the scaling description of elastic properties in our network model. In Sec. III we describe the techniques used to simulate this model numerically. In Sec. IV we present the results of the simulations, and in Sec. V we discuss some implications of these results and the conclusions that may be drawn therefrom. In the Appendix we provide details of the transfer-matrix method used to perform the simulations.

II. ELASTIC NETWORK MODEL AND SCALING THEORY

In order to discuss and simulate the critical behavior of a random, macroscopically inhomogeneous elastic solid near its rigidity threshold, we always consider a two-component random network of bonds with two types of microscopic force constants—a bond-stretching constant k and an angle-bending constant m . The bond-stretching constant takes one of two values k_1, k_2 according to the type of bond. The value of the angle-bending constant can in principle take more than two different values: First of all it depends on the character of its pair of adjacent bonds, of which there are three possible configurations (i.e., we can have m_{11}, m_{22}, m_{12}). Secondly, more than one type of interbond angle is often possible, as in a triangular network. It is probably not crucial exactly how we assign the angle-bending force constants, as long as we keep m_{11}/k_1 and m_{22}/k_2 finite.

It is also probably not important for the critical properties precisely what type of network we use—this is the principle of universality which governs all known critical points. Therefore, in order to keep the microphysics as simple as possible, we did all our calculations on a honeycomb network in which each bond is chosen randomly and independently to be either k_1 or k_2 . There is only one type of interbond angle, and the angle-bending constants are m_2 if both adjacent bonds are k_2 , and m_1 otherwise.

A homogeneous network of this type will have isotropic elastic properties, and the macroscopic bulk stiffness and shear moduli, κ and μ , are given in terms of the elementary force constants by

$$\kappa = \frac{k}{2\sqrt{3}}, \quad \mu = \frac{2\sqrt{3}km}{k+6m}. \quad (2.1)$$

We also note here that the $C_{11} \equiv C_{xxxx}$ modulus, which appears in the longitudinal sound velocity, is related to κ and μ in two-dimensional isotropic elastic materials by

$$C_{11} = \kappa + \mu. \quad (2.2)$$

Another important parameter which characterizes the elastic behavior of an isotropic material is Poisson's ratio Σ . In a two-dimensional medium, Σ is related to ratios of the elastic moduli in the following ways:

$$\Sigma = \frac{\kappa - \mu}{\kappa + \mu} = 1 - \frac{2\mu}{C_{11}}. \quad (2.3)$$

Since mechanical stability requirements dictate that κ and μ must be positive, therefore Σ must lie between -1 and $+1$ (in a two-dimensional medium). In our homogeneous network model, Σ is related to the microscopic force constants k, m by

$$\Sigma = \frac{k - 6m}{k + 18m}. \quad (2.4)$$

Since mechanical stability requires that k and m be positive, Σ in this model can take any value between $-\frac{1}{3}$ and $+1$. Although our model cannot reproduce all the allowed values for Σ , it is adequate for representing any natural material since all naturally occurring materials always have $\Sigma > 0$.

In a random inhomogeneous network, the bulk moduli will depend on the four force constants k_1, m_1, k_2, m_2 and also on the fraction p_1 of k_1 bonds. A sharp rigidity threshold appears in a system of infinite size when $k_1/k_2 = m_1/m_2 = 0$ and $p_2 = p_c$, where p_c is the percolation threshold. Near that threshold, the critical properties of the stiffness moduli are expected to exhibit scaling behavior. In preparation for a discussion of our computer simulations of finite networks at p_c , we proceed to make scaling Ansätze for such networks.

We first recall the scaling theory of the bulk effective conductivity σ_e of an infinitely large network with component conductivities $\sigma_1 < \sigma_2$ and $p_2 \neq p_c$ (see, e.g., Ref. 15). The scaling Ansatz is then

$$\sigma_e = \sigma_1 |p_2 - p_c|^{-s} g \left(\frac{\sigma_1/\sigma_2}{|p_2 - p_c|^{t+s}} \right), \quad (2.5)$$

where the scaling function has different forms g_+, g_- above and below p_c . This difference is preserved even in the other limit where the size L is finite and $p_2 = p_c$. In that case the correlation length $\xi \sim |p_2 - p_c|^{-\nu}$ is replaced everywhere by L , and the scaling Ansatz becomes (see Refs. 16–18 for a discussion of the finite-size scaling idea)

$$\sigma_e = \sigma_1 L^{s/\nu} G(\bar{\sigma}), \quad (2.6)$$

where

$$\bar{\sigma} = \frac{\sigma_1/\sigma_2}{L^{-(t+s)/\nu}}. \quad (2.7)$$

We shall be concerned with systems where $p_2 \rightarrow p_c^-$, i.e., from below, which is appropriate to the discussion of a superconductor-normal conductor mixture or a rigid-normal elastic mixture. In that case, when $\bar{\sigma} \ll 1$, the effective conductivity is independent of the conductivity of the superconducting bonds σ_2 , and G becomes a constant of order one. Thus the effective conductivity scales as

$$\sigma_e = \sigma_1 L^{s/\nu}. \quad (2.8)$$

In the other limit $\bar{\sigma} \gg 1$, the effective conductivity must be independent of L and therefore the function G must be proportional to $\bar{\sigma}^{-s/(t+s)}$, so that we get

$$\sigma_e = \sigma_1^{t/(t+s)} \sigma_2^{s/(t+s)}. \quad (2.9)$$

By analogy with the above discussion, we expected that the effective elastic moduli of the mixture $C_{11}^{(e)}$ and μ_e would be of the form

$$C_{11}^{(e)} = C_{11}^{(1)} L^{S/\nu} F(\bar{m}, \bar{k}, k_1/m_1), \quad (2.10a)$$

$$\mu_e = \mu_1 L^{S/\nu} \mathcal{F}(\bar{m}, \bar{k}, k_1/m_1), \quad (2.10b)$$

with

$$\bar{m} = \frac{m_1/m_2}{L^{-(T+S)/\nu}}, \quad (2.11a)$$

$$\bar{k} = \frac{k_1/k_2}{L^{-(T'+S)/\nu}}. \quad (2.11b)$$

The indices 1,2 refer to the normal and rigid components respectively. Thus we will always have $k_1 < k_2$, $m_1 < m_2$, $C_{11}^{(1)} < C_{11}^{(2)}$, $\mu_1 < \mu_2$. The moduli $C_{11}^{(i)}, \mu_i$ are the macroscopic stiffness moduli of a homogeneous network with the microscopic force constants k_i, m_i . Here we allowed F and \mathcal{F} to be functions of k_1/m_1 and of the scaling variables \bar{m} and \bar{k} . The values of the exponents T and T' will be determined later from our simulations. Originally, we had expected to find that $T = T'$, but we shall see that the results do not confirm this. Instead we shall see that $T \simeq 3.96$ and $T' \simeq 1.3$. In order to study the case where either \bar{m} or \bar{k} is very small or very large, we will study the dependence of F and \mathcal{F} either only on \bar{m} or only on \bar{k} , the other scaling parameter, as well as k_1/m_1 , being held fixed. In particular we will study four extreme limiting cases, namely,

$$\bar{m} \ll 1 \text{ and } \bar{k} \ll 1, \quad (2.12a)$$

$$\bar{m} \ll 1 \text{ and } \bar{k} \gg 1, \quad (2.12b)$$

$$\bar{m} \gg 1 \text{ and } \bar{k} \ll 1, \quad (2.12c)$$

$$\bar{m} \gg 1 \text{ and } \bar{k} \gg 1. \quad (2.12d)$$

As in the conductivity problem, where when $\bar{\sigma} \ll 1$, G becomes independent of σ_2 , we now expect that when $\bar{m} \ll 1$ the functions F and \mathcal{F} will be independent of \bar{m} , but may still depend on the other scaling variable \bar{k} and on the ratio k_1/m_1 . This can be understood intuitively by noting that when $\bar{m} \ll 1$, the effective stiffness moduli should not depend on the rigid angle-bending force constant m_2 but could still be a function of the variable rigid stretching force constant k_2

$$F(\bar{m}, \bar{k}, k_1/m_1) \rightarrow H(\bar{k}, k_1/m_1), \quad (2.13a)$$

$$\mathcal{F}(\bar{m}, \bar{k}, k_1/m_1) \rightarrow \mathcal{H}(\bar{k}, k_1/m_1), \quad (2.13b)$$

so that

$$C_{11}^{(e)} = C_{11}^{(1)} L^{S/\nu} H(\bar{k}, k_1/m_1), \quad (2.14a)$$

$$\mu_e = \mu_1 L^{S/\nu} \mathcal{H}(\bar{k}, k_1/m_1). \quad (2.14b)$$

Similarly, we expect that when $\bar{k} \ll 1$, the functions F and \mathcal{F} are independent of \bar{k} but may still depend on the other scaling variable \bar{m} and on the ratio k_1/m_1 . Again it can be understood intuitively by noting that when $\bar{k} \ll 1$, the effective stiffness moduli should not depend on the rigid bond-stretching force constant k_2 but can still be a function of the variable rigid angle-bending force constant m_2

$$F(\bar{m}, \bar{k}, k_1/m_1) \rightarrow X(\bar{m}, k_1/m_1), \quad (2.15a)$$

$$\mathcal{F}(\bar{m}, \bar{k}, k_1/m_1) \rightarrow \mathcal{X}(\bar{m}, k_1/m_1), \quad (2.15b)$$

so that

$$C_{11}^{(e)} = C_{11}^{(1)} L^{S/\nu} X(\bar{m}, k_1/m_1), \quad (2.16a)$$

$$\mu_e = \mu_1 L^{S/\nu} \mathcal{X}(\bar{m}, k_1/m_1). \quad (2.16b)$$

We now discuss the four extreme cases of Eqs. (2.12). By analogy with the conductivity problem when $\bar{\sigma} \ll 1$, we expect that when both $\bar{m} \ll 1$ and $\bar{k} \ll 1$, the effective stiffness moduli are independent of m_2 and k_2 and the functions F and \mathcal{F} depend only on the ratio k_1/m_1 ,

$$\begin{aligned} F(\bar{m}, \bar{k}, k_1/m_1) &\simeq H(\bar{k}, k_1/m_1) \\ &\simeq X(\bar{m}, k_1/m_1) \simeq W(k_1/m_1), \end{aligned} \quad (2.17a)$$

$$\begin{aligned} \mathcal{F}(\bar{m}, \bar{k}, k_1/m_1) &\simeq \mathcal{H}(\bar{k}, k_1/m_1) \\ &\simeq \mathcal{X}(\bar{m}, k_1/m_1) \simeq \mathcal{W}(k_1/m_1), \end{aligned} \quad (2.17b)$$

so that

$$C_{11}^{(e)} \simeq C_{11}^{(1)} L^{S/\nu} W(k_1/m_1) \simeq \mu_1 L^{S/\nu} A, \quad (2.18a)$$

$$\mu_e \simeq \mu_1 L^{S/\nu} \mathcal{W}(k_1/m_1) \simeq \mu_1 L^{S/\nu} B. \quad (2.18b)$$

The last form on the right-hand side (rhs) of these equations, in which A, B are constants, does not follow from any scaling assumption—it is a consequence of our simu-

lations to be explained in Sec. IV below.

If one of our scaling variables is very small while the other is very large, the effective elastic moduli are expected to be independent of the small variable and of the size as well. Thus, if $\bar{m} \ll 1$ while $\bar{k} \gg 1$, the effective moduli should depend on \bar{k} and on the ratio k_1/m_1 , but not on \bar{m} or L . We must therefore have

$$\begin{aligned} F(\bar{m}, \bar{k}, k_1/m_1) &\simeq H(\bar{k}, k_1/m_1) \\ &\simeq \bar{k}^{-S/(T+S)} Q(k_1/m_1), \end{aligned} \quad (2.19a)$$

$$\begin{aligned} \mathcal{F}(\bar{m}, \bar{k}, k_1/m_1) &\simeq \mathcal{H}(\bar{k}, k_1/m_1) \\ &\simeq \bar{k}^{-S/(T+S)} Q(k_1/m_1), \end{aligned} \quad (2.19b)$$

so that

$$C_{11}^{(e)} \simeq C_{11}^{(1)} Q(k_1/m_1) (k_1/k_2)^{-S/(T+S)}, \quad (2.20a)$$

$$\mu_e \simeq \mu_1 Q(k_1/m_1) (k_1/k_2)^{-S/(T+S)}. \quad (2.20b)$$

Similarly, if $\bar{k} \ll 1$, while $\bar{m} \gg 1$, the effective moduli should depend on \bar{m} and on the ratio k_1/m_1 , but not on \bar{k} or on L . We must then have

$$\begin{aligned} F(\bar{m}, \bar{k}, k_1/m_1) &\simeq X(\bar{m}, k_1/m_1) \\ &\simeq \bar{m}^{-S/(T+S)} Y(k_1/m_1), \end{aligned} \quad (2.21a)$$

$$\begin{aligned} \mathcal{F}(\bar{m}, \bar{k}, k_1/m_1) &\simeq \mathcal{X}(\bar{m}, k_1/m_1) \\ &\simeq \bar{m}^{-S/(T+S)} \mathcal{Y}(k_1/m_1), \end{aligned} \quad (2.21b)$$

so that

$$C_{11}^{(e)} \simeq C_{11}^{(1)} Y(k_1/m_1) (m_1/m_2)^{-S/(T+S)}, \quad (2.22a)$$

$$\mu_e \simeq \mu_1 \mathcal{Y}(k_1/m_1) (m_1/m_2)^{-S/(T+S)}. \quad (2.22b)$$

When both $\bar{m} \gg 1$ and $\bar{k} \gg 1$, the effective elastic moduli should be independent of L . For this to happen, the functions F and \mathcal{F} must become homogeneous functions of appropriate powers of the scaling variables in this regime, i.e.,

$$\begin{aligned} F(\bar{m}, \bar{k}, k_1/m_1) &\rightarrow \bar{k}^{-S/(T+S)} f(\bar{k}^{T+S} \bar{m}^{T+S}, k_1/m_1), \\ & \quad (2.23a) \end{aligned}$$

$$\begin{aligned} \mathcal{F}(\bar{m}, \bar{k}, k_1/m_1) &\rightarrow \bar{k}^{-S/(T+S)} \mathcal{A}(\bar{k}^{T+S} \bar{m}^{T+S}, k_1/m_1). \\ & \quad (2.23b) \end{aligned}$$

From this we get

$$\begin{aligned} C_{11}^{(e)} &\sim C_{11}^{(1)} \left[\frac{k_1}{k_2} \right]^{-S/(T+S)} \\ &\quad \times f((k_1/k_2)^{T+S} (m_2/m_1)^{T+S}, k_1/m_1), \end{aligned} \quad (2.24a)$$

$$\begin{aligned} \mu_e &\sim \mu_1 \left[\frac{k_1}{k_2} \right]^{-S/(T+S)} \\ &\quad \times \mathcal{A}((k_1/k_2)^{T+S} (m_2/m_1)^{T+S}, k_1/m_1). \end{aligned} \quad (2.24b)$$

In Sec. IV below we shall present evidence to indicate

that f, \neq are independent of their first argument and depend only on k_1/m_1 .

III. NUMERICAL SIMULATIONS—TECHNIQUE

As mentioned previously, the model for simulations is a two-dimensional (2D) honeycomb network of elastic bonds. Every bond has a bond-stretching force constant k and every pair of adjacent bonds have an angle-bending force constant m . The elastic potential energy can thus be written as

$$V = \sum_i \frac{1}{2} k_i \delta b_i^2 + \sum_{(i,j)=NN} \frac{1}{2} m_{ij} \delta \phi_{ij}^2, \tag{3.1}$$

where δb_i is the change in length of the bond i while $\delta \phi_{ij}$ is the change in the angle between the nearest-neighbor (NN) bonds i and j .

Every bond is chosen independently and randomly to be either a “normal bond” with a probability p_1 and a stretching force constant k_1 or a “rigid bond” with a probability $p_2 = 1 - p_1$ and a stretching force constant $k_2 \gg k_1$. Furthermore, the angle-bending force constant between a pair of adjacent rigid bonds is m_2 , while any other pair of adjacent bonds has the bending constant $m_1 \ll m_2$. This model has the property that the percolation threshold of the rigid bonds $p_2 = p_c$ is the same as the rigidity threshold of the network. This threshold is known exactly to be $p_c = 1 - 2 \sin(\pi/18) \approx 0.65270$.¹⁹

The method used to solve for the macroscopic elastic properties of this network was the transfer-matrix method. This method is most appropriate when the system has the shape of a long strip with a fixed width L_x . The response of the strip to external forces which are imposed at the sites at one end is determined by the elastic compliance matrix B_{ij} in the form

$$u_i = \sum_j B_{ij} f_j. \tag{3.2}$$

Here f_j ranges over both components of the external forces applied at all the sites of the two right-hand columns of the strip, while u_i ranges over both components of the resulting displacements at the same sites (see Fig. 1). Starting off with $B_{ij} \equiv 0$, bonds are added to the strip in triplets, and the matrix B_{ij} is recalculated at each step: As new bonds are added, new sites appear and correspondingly new elements of this matrix also appear. At the same time, an element B_{ij} can be discarded as soon as the site i or j becomes an internal site, i.e., as soon as the total internal force exerted upon it can be calculated entirely in terms of the displacements at existing sites. Since the total internal force must vanish at equilibrium, we can eliminate all elements of B_{ij} connected to that site. The basic procedure and equations for doing that are described in more detail in the Appendix. Thus the size of the compliance matrix B does not change when new sites and bonds are added to the strip, and we can gradually increase the length of the strip L_y up to a size that is only limited by the computing time that is available. Moreover, this process can be interrupted at any point and continued at a later time—all we must do is retain the matrix elements B_{ij} and the information

about the bonds in the last two columns.

In order to calculate the macroscopic stiffness moduli, it is necessary to impose appropriate boundary conditions at the edges of the network. At the two long edges we simply make the system periodic, so that it becomes effectively infinite but periodic in the x direction. The choice of $B_{ij} = 0$ at the beginning of the strip is equivalent to applying zero displacements there. At the other end of the strip we add a whole column of rigid triplets. As a result, all the displacements of sites at that end will be identical, and any element of B_{ij} will then give us the ra-

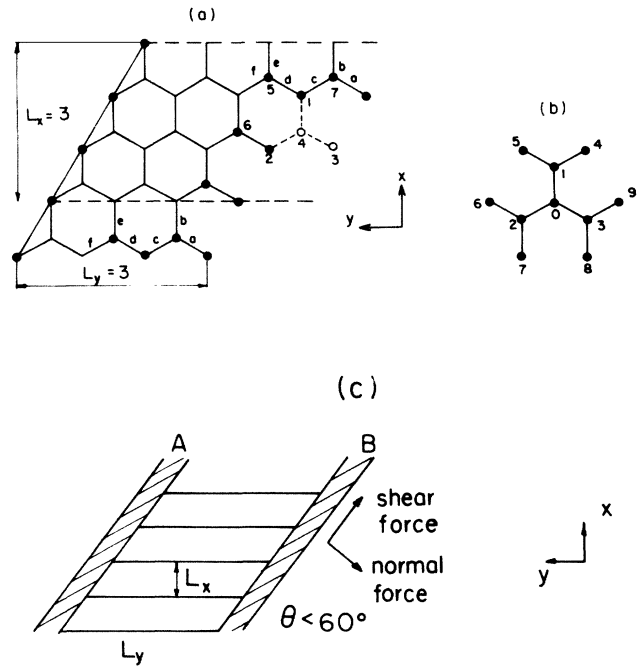


FIG. 1. (a) Section of an $L_x \times L_y$ strip of a honeycomb network. The network is extended periodically outside the two dashed lines so that the bonds $a-f$ from the top row of cells reappear below the bottom row as shown. The compliance matrix B_{ij} relates $(x$ and $y)$ displacements u_i to the $(x$ and $y)$ forces f_i applied at each of the \bullet -shaped sites at the two right-hand columns. The sites at the left edge of the strip are permanently tied to a rigid bar which is held fixed. The sites at the right edge are also tied to a rigid bar every time it is desired to calculate the macroscopic moduli. The dashed bonds and open circles \circ represent bonds and sites that are in the process of being added to the network. The numbered sites are the sites where additional forces appear as a consequence of the new force constants that are added. The new sites 3,4 replace the sites 1,5 as indices of the compliance matrix. These site numbers refer to Eqs. (A3)–(A12) and are unrelated to the site numbers in (b). (b) The piece of the network that must be considered when calculating all the internal forces that act at the central site (0). The site numbers here refer to Eqs. (A1) and (A2) and are unrelated to the site numbers in (a). (c) Schematic picture of the periodically extended network sandwiched between two rigid bars A and B . The bars are parallel and extend to infinity in both directions, as does the network between them. They are inclined at an angle θ with respect to the y axis, where θ is given by Eq. (A15) and tends to 60° as the period $L_x \rightarrow \infty$.

tion between a macroscopic displacement and a macroscopic force. Due to the expected isotropy of the macroscopic elastic properties, we can expect just two types of nonzero elements of this matrix, leading to two independent bulk stiffness moduli

$$C_{11}^{(e)} = C_{xxxx}^{(e)} = (f_y/L_x)/(u_y/L_y), \tag{3.3a}$$

$$\mu_e = C_{xyxy}^{(e)} = (f_x/L_x)/(u_x/L_y). \tag{3.3b}$$

These expressions assume that the strip has an overall rectangular shape. In fact, due to the method of construction and the method of implementing the macroscopic periodicity, the rigid columns at the end of the strip are inclined at an angle θ with respect to the y axis that depends on L_x and tends to 60° as $L_x \rightarrow \infty$ [see Fig. 1(c)]. Corresponding changes must be made in relating the matrix elements B_{ij} at the end of the strip to the bulk moduli. Those details are described in the Appendix.

Applying the macroscopic external forces and displacements at the short edge of the strip is appropriate for simulations of a rigid-normal mixture at $p_2 \leq p_c$, since there will always be rigid clusters that percolate in the x direction if L_y is large enough, but there will be no such clusters that percolate in the y direction. Measurements of the macroscopic elastic moduli in the way we have described will thus be dominated by the force constants of the normal component k_1, m_1 . By contrast, measurements made by applying the external forces and displacements at the long edges would be dominated by the force constants of the rigid component k_2, m_2 . That would be appropriate for determining the form of the scaling functions above the threshold, i.e., for $p_2 \geq p_c$. However, this is not the subject of the present paper. The periodic boundary conditions applied in the x direction are intended to ensure that as far as the macroscopic behavior is concerned, the network is like an infinitely long strip held between two parallel and infinitely long rigid bars. The bars and the strip are oriented at an angle $\theta \simeq 60^\circ$ with the y axis, and the width of the strip is finite but very large, i.e., proportional to L_y . If instead we had left the long edges free (i.e., with a zero-force boundary condition), we would only have been able to measure a single macroscopic modulus, namely, Young's modulus. Some of these considerations are analogous to those that were made when the transfer matrix method was applied to the simulation of random conductor networks in the form of long strips.^{20,21} The case discussed here is obviously the analogue of the superconductor-normal conductor mixture.

IV. NUMERICAL SIMULATIONS—RESULTS AND IMPLICATIONS

As a starting point in the analysis of our results it is important to study Fig. 2, where we plot $C_{11}^{(e)}/L^{S/\nu}$ (throughout this section we use L to represent the strip width L_x) and $\mu_e/L^{S/\nu}$ as functions of L for $m_1/m_2 = 10^{-9}$ and $k_1/k_2 = 10^{-7}$. We found that these plots are most nearly constant if we choose

$$S = 1.15, \quad \nu = \frac{4}{3}. \tag{4.1}$$

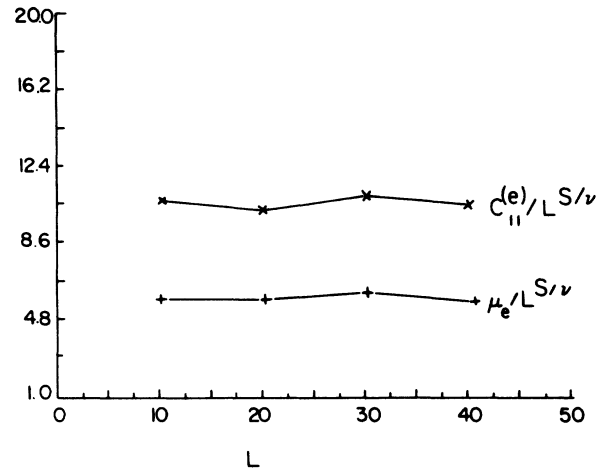


FIG. 2. Values of $C_{11}^{(e)}/L^{S/\nu}$ (\times) and $\mu_e/L^{S/\nu}$ ($+$) plotted vs L , with $S = 1.15$ and $\nu = \frac{4}{3}$, for $k_2 = 10^7 k_1$, $m_2 = 10^9 m_1$, and $k_1/m_1 = 15.82$. Two lines were drawn through the points in order to guide the eye.

This value of S is significantly lower than the value $S = 1.30$ found in Ref. 13 even when we take into account the statistical errors. Already in Ref. 13 it was found that very long strips are needed before the asymptotic behavior is reached: $L_y = 40\,000$ was far from being long enough for $L_x = 40$. In our calculations the strip lengths for comparable widths were even shorter, and that is probably the reason for the poor quality of the asymptotic behavior.

In the simulations we decided to study the behavior of the elastic moduli as we varied one of ratios of the microscopic elastic force constants k_1, k_2, m_1 , and m_2 while keeping the others fixed. This was done in three different ways, each time allowing a different ratio to vary and keeping another ratio constant and very small:

Case	Very small constant	Variable
1	m_1/m_2	k_1/k_2
2	k_1/k_2	m_1/m_2
3		$m_1/m_2 = k_1/k_2$.

In the first case the bulk moduli should scale as Eqs. (2.14) and in the limits when $\bar{k} \ll 1$ and $\bar{k} \gg 1$ the behavior will be given by Eqs. (2.18) and (2.20), respectively. In the second case the bulk moduli should scale as Eqs. (2.16) and when $\bar{m} \ll 1$ and $\bar{m} \gg 1$ the behavior will be given by Eqs. (2.18) and (2.22). In the third case the bulk moduli should scale as Eqs. (2.10) in the particular case where the microscopic elastic force constants satisfy $m_1/m_2 = k_1/k_2$, and in the limits $\bar{m}, \bar{k} \ll 1$ and $\bar{m}, \bar{k} \gg 1$ the behavior will be given by Eqs. (2.18) and (2.24). Clearly the three cases reach a common limit when both scaling variables are much smaller than one. The behavior is then described by Eqs. (2.18).

For each of these cases the results of our simulations are presented in three forms. First we exhibit the macroscopic moduli $C_{11}^{(e)}, \mu_e$ and their ratio $\mu_e/C_{11}^{(e)}$ versus the

appropriate variable parameter k_1/k_2 or m_1/m_2 over the entire range of the calculations (see Figs. 3, 6, and 9).

Then, in order to study the scaling assumptions in the limit that both scaling variables are very small, we exhibit the elastic moduli divided by $L^{S/\nu}$ versus the relevant scaling variable \tilde{k} or \tilde{m} . From (2.18) this is expected to be approximately constant when both $\tilde{k}, \tilde{m} \ll 1$, and also independent of L (see Figs. 4, 7, and 10–12).

Finally, in the limit when at least one of the scaling variables \tilde{k} or \tilde{m} is very large we exhibit the effective elastic moduli divided by the appropriate power of the ratio k_1/k_2 (or m_1/m_2) that is expected to make the result independent of that ratio, as well as of L (see Figs. 5, 8, and 13).

Case 1. We study the case when $\tilde{m} \ll 1, m_1/m_2$ is

fixed at 10^{-9} , and k_1/k_2 varies in the range $10^{-9} \leq k_1/k_2 \leq 1$. In particular, we chose the force constants as follows:

$$k_1 = 6.2984, \quad m_1 = 0.39817, \quad k_1/m_1 = 15.82,$$

$$k_2 = \text{variable}, \quad m_2 = 10^9 m_1.$$

The values of k_1, m_1 were chosen so as to make the bulk moduli of the normal component have the values [see Eqs. (2.1) and (2.2)]

$$\kappa_1 = 1.8182, \quad \mu_1 = 1.0, \quad C_{11}^{(1)} = 2.8182.$$

In Fig. 3 we present the effective elastic moduli $C_{11}^{(e)}$ and μ_e as well as their ratio $\mu_e/C_{11}^{(e)}$ as functions of the

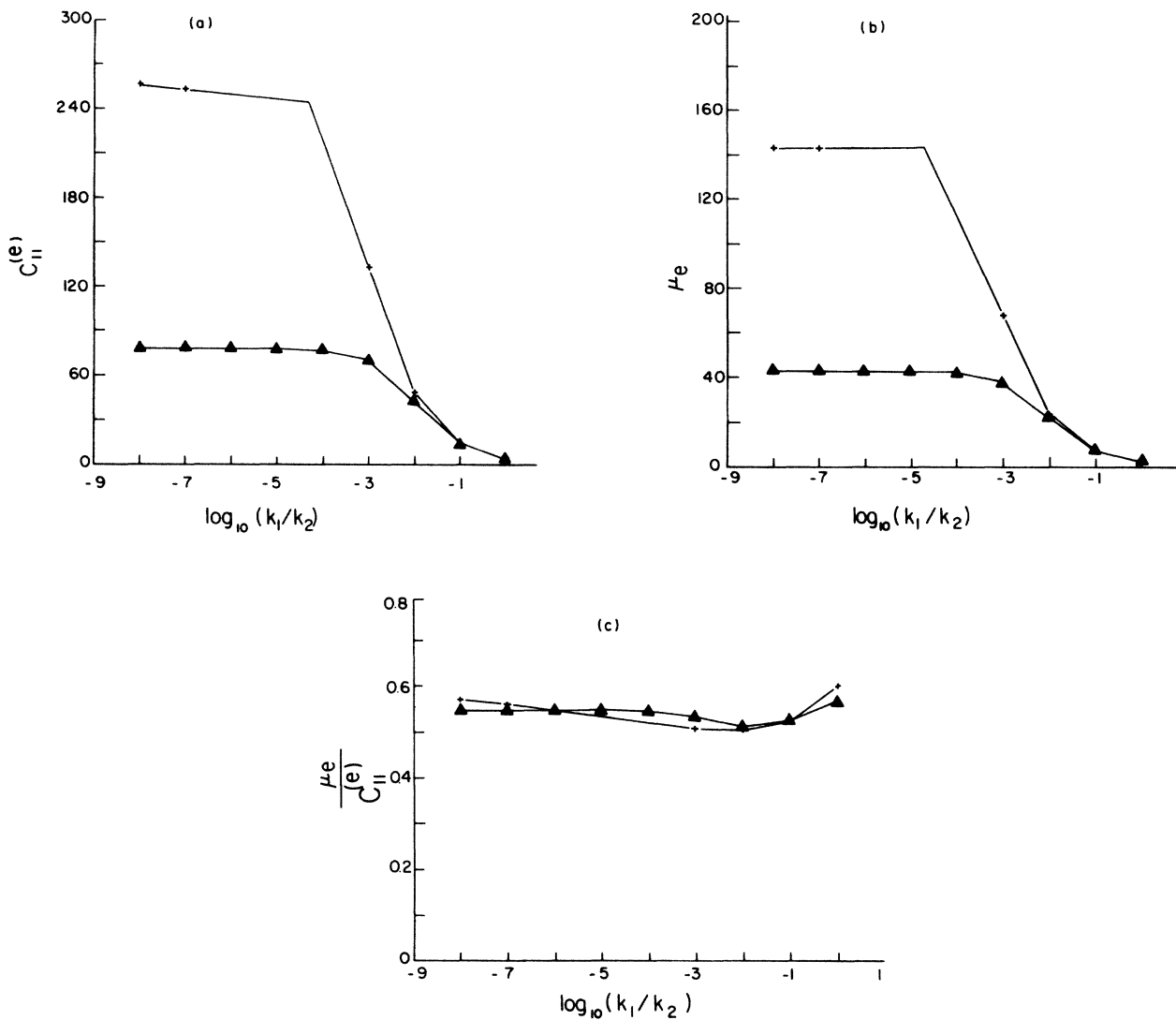


FIG. 3. (a) Values of $C_{11}^{(e)}$ plotted vs $\log_{10}(k_1/k_2)$. The points are the numerical simulation results for $L = 10$ (\blacktriangle) and 40 ($+$), with $k_1/m_1 = 15.82$. The lines were drawn through the points to guide the eye. (b) Values of μ_e plotted vs $\log_{10}(k_1/k_2)$. The points are the numerical simulation results for $L = 10$ (\blacktriangle) and 40 ($+$), with $k_1/m_1 = 15.82$. The lines were drawn through the points to guide the eye. (c) Values of the ratio $\mu_e/C_{11}^{(e)}$ plotted vs $\log_{10}(k_1/k_2)$. The points are the numerical simulation results for $L = 10$ (\blacktriangle) and 40 ($+$), with $k_1/m_1 = 15.82$. The lines were drawn through the points to guide the eye.

ratio of the microscopic elastic force constants k_1/k_2 , for $L = 10$ and 40 . From Figs. 3(a) and 3(b), we see that the elastic moduli have a strong L dependence, and from Fig. 3(c), we see that this gets cancelled out when we calculate the ratio $\mu_e/C_{11}^{(e)}$. From Fig. 3(c) we also see that all the values of $\mu_e/C_{11}^{(e)}$ lie above 0.5, and consequently Poisson's ratio Σ_e is negative [see Eq. (2.3)]. In the limit of large k_2 , where the results for the macroscopic moduli depend only on k_1 and m_1 (since m_2 is also very large), this negative value of Σ_e is known to be independent event of k_1 and m_1 .¹³ In fact, it is easy to see from Eq. (2.4) that our choice of k_1, m_1 corresponds to the positive value $\Sigma_1 = 0.29$. In the other limit, where the results for μ_e and $C_{11}^{(e)}$ depend on k_2 , the negative values of Σ_e changed to positive values when we repeated the simulations using a smaller fixed value for m_2 , namely $m_2 = 10^4 m_1$.

The same results but with rescaled axes are plotted in Fig. 4, where we present the elastic moduli divided by $L^{S/\nu}$ as a function of the scaling variable \tilde{k} , for $T' = 1.30$ and $S = 1.30$ (see the solid lines in these figures). We observe that in the region of very small \tilde{k} , where both scaling variables are very small, the rescaled moduli are approximately independent of L and \tilde{k} in agreement with Eqs. (2.18). Also over the entire range of \tilde{k} that was studied the curves for $L = 10$ and 40 lie close to each other and follow a single function of \tilde{k} , in agreement with Eqs. (2.14). In fact we chose the value of $S = 1.30$ and fitted the value of T' so as to get good agreement between the results of the simulations and the scaling assumption. The result was that T' is equal to the t exponent of the conductivity problem (i.e., $T' = 1.3$), but is very different from the value of 3.96. This result may perhaps be understood as follows: The exponent T' only becomes important in the scaling behavior when the moduli change with \tilde{k} and this occurs only when $k_1/k_2 \geq 10^{-4}$. Under these conditions, the rigid component, while having a very large value of $m_2 \approx 10^8$, has a much smaller value of $k_2 < 10^5$. It is thus conceivable that even though the rigid angles remain unchanged, the rigid-bond lengths do get changed and make a major contribution to the macroscopic behavior which is more important than that of the nonpercolating normal bonds. This contribution, since it involves only bond length deformations, can reasonably be expected to behave near p_c like the bulk conductivity.

In Fig. 5 we plot the same results but rescaled in a different way: The elastic moduli are divided by $(k_1/k_2)^{S/(T'+S)}$ in accordance with Eqs. (2.20), for $T' = 1.30$ and $S = 1.30$ (see solid lines in these figures), and are plotted versus k_1/k_2 . We observe that in the region of very large k_1/k_2 , where $\tilde{m} \ll 1$ while $\tilde{k} \gg 1$, the rescaled moduli are approximately independent of L and k_1/k_2 , in agreement with Eqs. (2.20). This shows that the scaling assumptions are valid also for large values of \tilde{k} .

If we repeat the procedure leading to the solid lines of Figs. 4 and 5 assuming a different value of S , namely, $S = 1.15$ (as was found in Fig. 2) and fit T' to get the best scaling behavior we get plots that are slightly different from the solid lines of Figs. 4 and 5 and are emphasized

in Figs. 4 and 5 as dashed lines. From these new presentations of the same results we see that the scaling assumptions seem to work even better, and that the optimum value of T' is then $T' = 1.1$.

These observations indicate that precise values for the various exponents cannot be obtained from these simula-

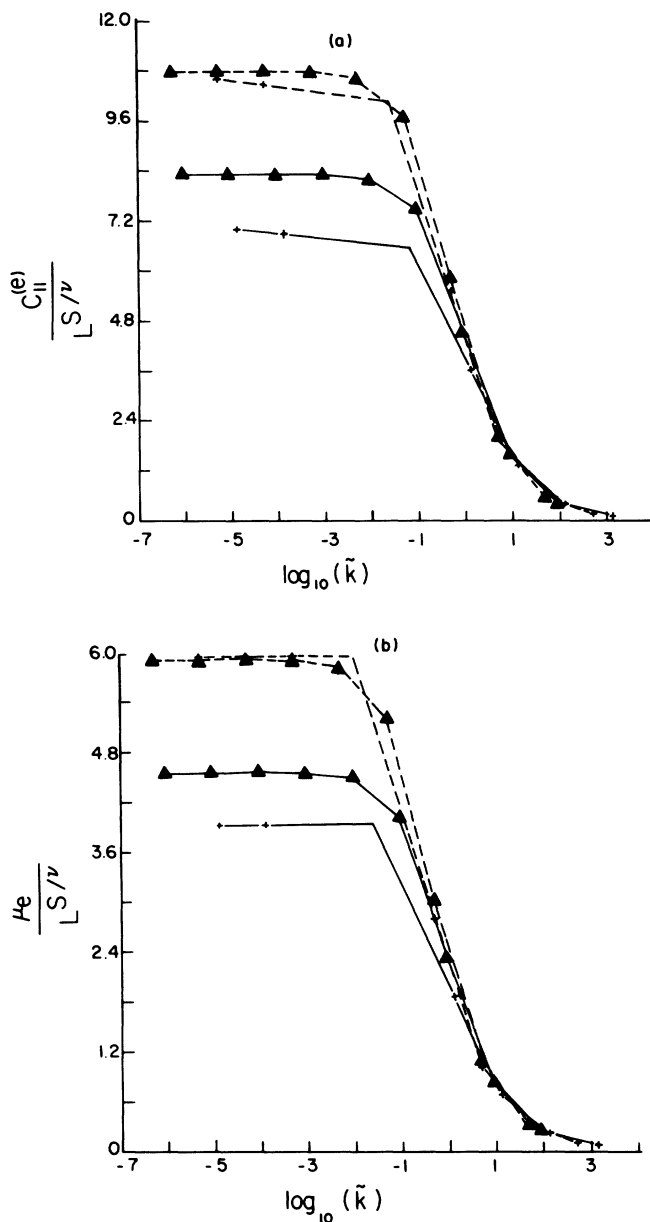


FIG. 4. (a) Values of $C_{11}^{(e)}/L^{S/\nu}$ plotted vs $\log_{10}(\tilde{k})$, for $k_1/m_1 = 15.82$. The points are the numerical simulation results for $L = 10$ (\blacktriangle) and 40 ($+$). The lines were drawn through the points to guide the eye and to differentiate between the results with $T' = 1.30$ and $S = 1.30$ (solid lines) and with $T' = 1.10$ and $S = 1.15$ (dashed lines). (b) Values of $\mu_e/L^{S/\nu}$ plotted vs $\log_{10}(\tilde{k})$, for $k_1/m_1 = 15.82$. The points are the numerical simulation results for $L = 10$ (\blacktriangle) and 40 ($+$). The lines were drawn through the points to guide the eye and to differentiate between the results with $T' = 1.30$ and $S = 1.30$ (solid lines) and with $T' = 1.10$ and $S = 1.15$ (dashed lines).

tions. For that purpose a more careful study would have to be undertaken that would include longer strips and wider ranges of the scaling variables.

Case 2. We study the case when $\bar{k} \ll 1$, k_1/k_2 is fixed at 10^{-9} , and m_1/m_2 varies in the range $10^{-9} \leq m_1/m_2 \leq 1$. In particular, we chose the force con-

stants as follows:

$$k_1 = 6.2984, \quad m_1 = 0.39817, \quad k_1/m_1 = 15.82,$$

$$k_2 = 10^9 k_1, \quad m_2 = \text{variable}.$$

The bulk moduli of the normal component are as before.

In Fig. 6 we plot the bulk moduli $C_{11}^{(e)}$ and μ_e as well as their ratio $\mu_e/C_{11}^{(e)}$ versus the ratio m_1/m_2 for $L = 10$ and 40 . From Figs. 6(a) and 6(b), we see that the elastic moduli again have a strong L dependence which gets cancelled when the ratio $\mu_e/C_{11}^{(e)}$ is calculated. In Fig. 6(c) we observe that $\mu_e/C_{11}^{(e)} < 0.5$ when $m_1/m_2 > 10^{-6}$ while $\mu_e/C_{11}^{(e)} > 0.5$ when $m_1/m_2 < 10^{-6}$. This is similar to what happened in Case I, where when $m_2 = 10^9 m_1$ we found $\mu_e/C_{11}^{(e)} > 0.5$ over the entire range of k_1/k_2 studied, but when $m_2 = m_1 \cdot 10^4$ we found $\mu_e/C_{11}^{(e)} > 0.5$ for $k_1/k_2 > 0.5$ and $\mu_e/C_{11}^{(e)} < 0.5$ for $k_1/k_2 < 0.06$.

The same results are replotted using rescaled axes in Fig. 7, where we present the elastic moduli divided by $L^{S/\nu}$ as a function of the scaling variable \bar{m} , with $T = 3.96$ and $S = 1.30$ (see solid lines). We observe that in the region of very small \bar{m} , where both scaling variables are very small, the rescaled moduli are approximately independent of L and \bar{m} , in agreement with Eqs. (2.18). Also, over the entire range of \bar{m} that was studied the curves for $L = 10$ and 40 lie close to each other, and follow a single function of \bar{m} , in agreement with Eqs. (2.16).

The same results are plotted a third time with yet a different rescaling in Fig. 8, where the elastic moduli divided by $(m_1/m_2)^{-S/(T+S)}$ are plotted versus m_1/m_2 . From Figs. 8(a) and 8(b) we see that for very large m_1/m_2 , where $\bar{k} \ll 1$ while $\bar{m} \gg 1$, the ratio $C_{11}^{(e)}/(m_1/m_2)^{-S/(T+S)}$ is approximately independent of L and of m_1/m_2 in agreement with Eqs. (2.20), while the ratio $\mu_e/(m_1/m_2)^{-S/(T+S)}$ is not constant. This shows that the scaling assumptions for the shear modulus μ_e work rather poorly. It might be necessary to introduce an additional exponent to explain the results when one of the scaling parameters is large. Additional attention was given to understand the results of Fig. 6 and we again tried to improve the fit shown by a solid line in Fig. 7, by choosing nonstandard values for S and T . Choosing $S = 1.15$ and $T = 2.9$ improved the fit in the case of $C_{11}^{(e)}$ but made it worse for μ_e . A better fit for μ_e was obtained by choosing $S = 1.3$ and $T = 2.9$ (see dashed line and dot-dashed line in Figs. 7 and 8). Again, a more careful and more extended study is needed before precise values for these exponents can be deduced from such simulations.

Case 3. We study the case when $m_1/m_2 = k_1/k_2$ and varies in the range $10^{-9} \leq m_1/m_2 = k_1/k_2 \leq 1$. In particular we chose two sets of force constants

$$k_1 = 2.1651, \quad m_1 = 1.4434, \quad k_1/m_1 = 1.5,$$

$$k_2 = \text{variable}, \quad m_2 = \frac{m_1}{k_1} k_2, \quad (4.2a)$$

$$\kappa_1 = 0.625, \quad \mu_1 = 1, \quad C_{11}^{(1)} = 1.625,$$

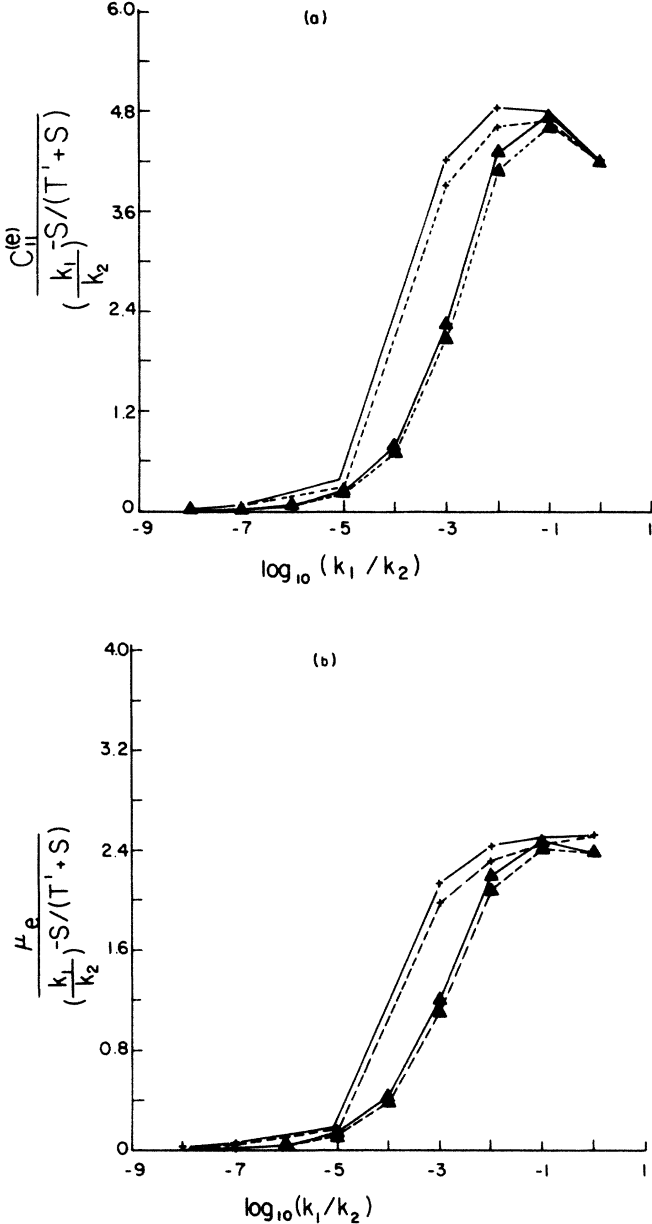


FIG. 5. (a) Values of $C_{11}^{(e)}/[(k_1/k_2)^{-S/(T+S)}]$ plotted vs $\log_{10}(k_1/k_2)$, with $k_1/m_1 = 15.82$ ($C_{11}^{(1)} = 2.8182$). The points are the numerical simulation results for $L = 10$ (▲) and 40 (+). The lines were drawn through the points to guide the eye and to differentiate between the results with $T' = 1.30$ and $S = 1.30$ (solid lines) and with $T' = 1.10$ and $S = 1.15$ (dashed lines). (b) Values of $\mu_e/[(k_1/k_2)^{-S/(T+S)}]$ plotted vs $\log_{10}(k_1/k_2)$, with $k_1/m_1 = 15.82$ ($\mu_1 = 1.0$). The points are the numerical simulation results for $L = 10$ (▲) and 40 (+). The lines were drawn through the points to guide the eye and to differentiate between the results with $T' = 1.30$ and $S = 1.30$ (solid lines) and with $T' = 1.10$ and $S = 1.15$ (dashed lines).

$$k_1 = 6.2984, \quad m_1 = 0.39817, \quad k_1/m_1 = 15.82,$$

$$k_2 = \text{variable}, \quad m_2 = \frac{m_1}{k_1} k_2, \quad (4.2b)$$

$$\kappa_1 = 1.8182, \quad \mu_1 = 1, \quad C_{11}^{(1)} = 2.8182.$$

In Fig. 9 we plot the bulk moduli $C_{11}^{(e)}$ and μ_e , as well as their ratio $\mu_e/C_{11}^{(e)}$ versus the ratio $m_1/m_2 = k_1/k_2$, for $L = 10$ and 40 , and for both parameter sets in Eqs. (4.2a) and (4.2b). From Fig. 9 we see that the elastic moduli have a strong L dependence that gets cancelled in the ratio $\mu_e/C_{11}^{(e)}$. In Fig. 9(c), we see again the tendency of $\mu_e/C_{11}^{(e)}$ to go above 0.5 (i.e., Σ_e becomes negative) when m_1/m_2 becomes very small. The same results but

with rescaled axes appear in Figs. 10 and 11 where we exhibit the two sets of elastic moduli divided by $L^{S/\nu}$ as a function \tilde{k} and \tilde{m} , with $T' = 1.3$ and $T = 3.96$, when $m_1/m_2 = k_1/k_2$. Note that when both scaling variables are very small, the rescaled moduli are approximately independent of L , \tilde{m} and \tilde{k} , in agreement with Eqs. (2.18), and for the entire range studied the curves for different L lie rather close to each other, so that it is difficult to decide which is the correct scaling variable.

For $\tilde{k} \gg 1$, \tilde{k} seems to be a better variable than \tilde{m} while for $\tilde{k} \ll 1$ both \tilde{k} and \tilde{m} are equally irrelevant since the scaled moduli tend to constant values. We further see from these figures that for very low values of \tilde{m} (or \tilde{k}), $C_{11}^{(e)}/L^{S/\nu}$ does not depend on the value of $C_{11}^{(1)}$. Since both sets of parameters include the same value of μ_1 , namely 1, we conclude that in this regime $C_{11}^{(e)}$ depends

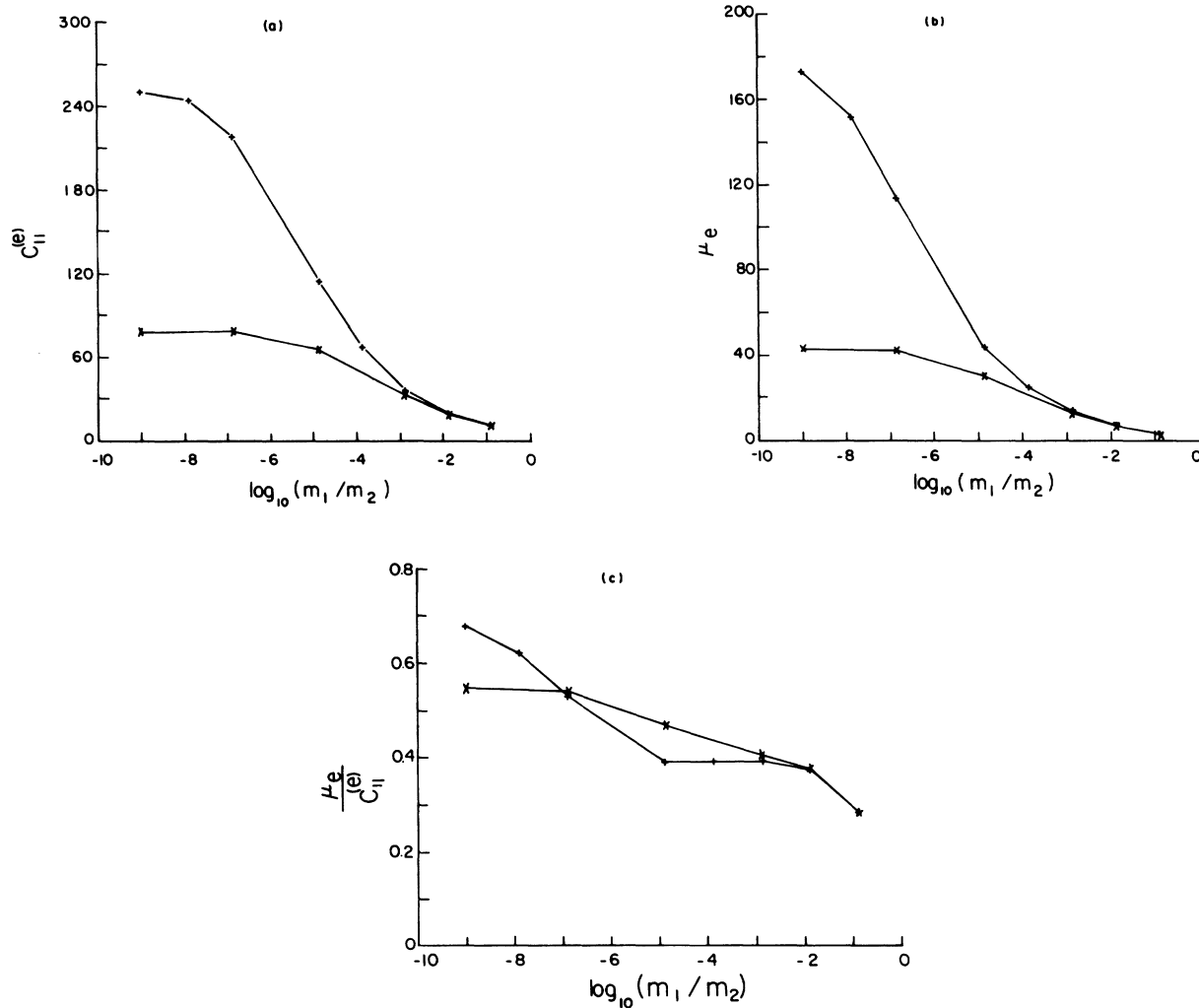


FIG. 6. (a) Values of $C_{11}^{(e)}$ plotted vs $\log_{10}(m_1/m_2)$. The points are the numerical simulation results for $L = 10$ (x) and 40 (+), with $k_1/m_1 = 15.82$. The lines were drawn through the points to guide the eye. (b) Values of μ_e plotted vs $\log_{10}(m_1/m_2)$. The points are the numerical simulation results for $L = 10$ (x) and 40 (+), with $k_1/m_1 = 15.82$. The lines were drawn through the points to guide the eye. (c) Values of the ratio $\mu_e/C_{11}^{(e)}$ plotted vs $\log_{10}(m_1/m_2)$. The points are the numerical simulation results for $L = 10$ (x) and 40 (+), with $k_1/m_1 = 15.82$. The lines were drawn through the points to guide the eye.

only on μ_1 . This was confirmed by additional simulations where different values of μ_1 were considered. This result forms the basis for the last forms on the rhs of Eqs. (2.18).

In Fig. 12 we again exhibit the rescaled variables $C_{11}^{(e)}/L^{S/\nu}$ and $\mu_e/L^{S/\nu}$ but with a different choice for S , namely $S=1.15$ (as we found from Fig. 2). Evidently,

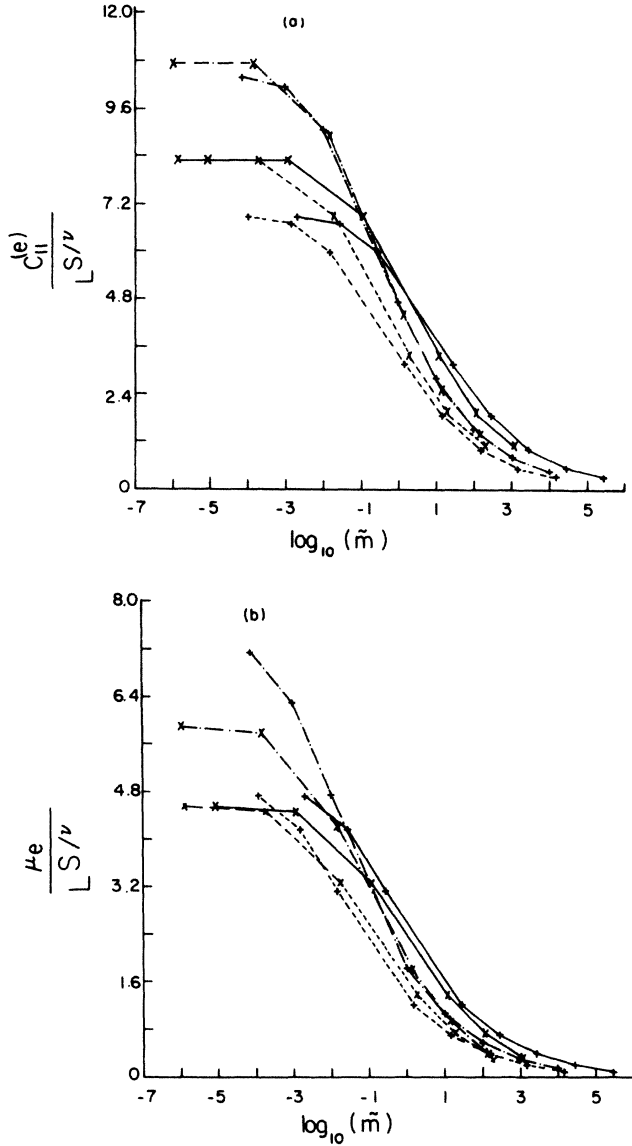


FIG. 7. (a) Values of $C_{11}^{(e)}/L^{S/\nu}$ plotted vs $\log_{10}(\tilde{m})$, with $k_1/m_1 = 15.82$. The points are the numerical simulation results for $L=10(\times)$ and $40(+)$. The lines were drawn through the points to guide the eye and to differentiate between the results with $T=3.96$ and $S=1.30$ (solid lines), with $T=2.90$ and $S=1.30$ (dashed lines) and with $T=2.90$ and $S=1.15$ (dot-dashed lines). (b) Values of $\mu_e/L^{S/\nu}$ plotted vs $\log_{10}(\tilde{m})$, with $k_1/m_1 = 15.82$. The points are the numerical simulation results for $L=10(\times)$ and $40(+)$. The lines were drawn through the points to guide the eye and to differentiate between the results with $T=3.96$ and $S=1.30$ (solid lines), with $T=2.90$ and $S=1.30$ (dashed lines) and with $T=2.90$ and $S=1.15$ (dot-dashed lines).

$C_{11}^{(e)}$ scales somewhat better for this choice but μ_e scales less well. It also serves to show how sensitive our results are to small changes in the values of the exponents.

The same results are plotted again but with a different rescaling in Fig. 13, where we show the elastic moduli divided by $[A(k_1/k_2)^{-S/(T+S)}]$ ($A=C_{11}^{(1)}$ or $A=\mu_1=1$)

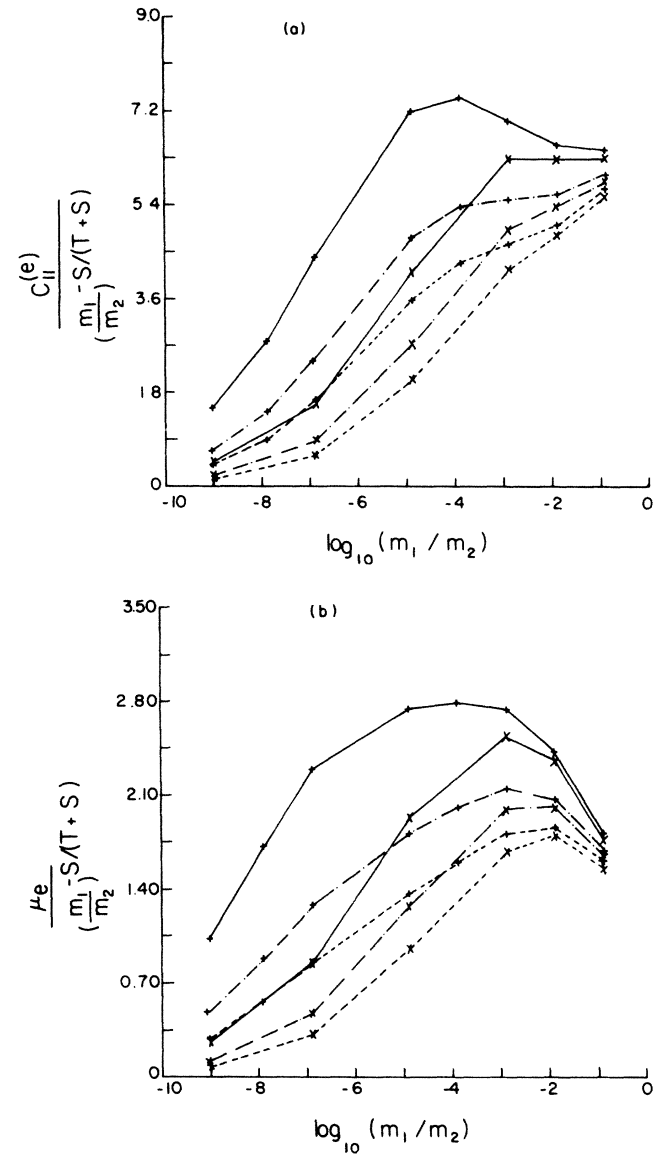


FIG. 8. (a) Values of $C_{11}^{(e)}/(m_1/m_2)^{S/(T+S)}$ plotted vs $\log_{10}(m_1/m_2)$, with $k_1/m_1 = 15.82$. The points are the numerical simulation results for $L=10(\times)$ and $40(+)$. The lines were drawn through the points to guide the eye and to differentiate between the results with $T=3.96$ and $S=1.30$ (solid lines), with $T=2.90$ and $S=1.30$ (dashed lines) and with $T=2.90$ and $S=1.15$ (dot-dashed lines). (b) Values of $\mu_e/(m_1/m_2)^{S/(T+S)}$ plotted vs $\log_{10}(m_1/m_2)$, with $k_1/m_1 = 15.82$. The points are the numerical simulation results for $L=10(\times)$ and $40(+)$. The lines were drawn through the points to guide the eye and to differentiate between the results with $T=3.96$ and $S=1.30$ (solid lines), with $T=2.90$ and $S=1.30$ (dashed lines) and with $T=2.90$ and $S=1.15$ (dot-dashed lines).

versus k_1/k_2 . In the region where both $k_1/k_2 = m_1/m_2$ are very large, the rescaled moduli are approximately independent of L and k_1/k_2 , in agreement with Eqs. (2.24) when f, ℓ depend only on k_1/m_1 . This indicates that the scaling assumptions are valid also when k_1/k_2 is very large, and that the asymptotic scaling functions f, ℓ are particularly simple.

Finally, let us consider the Figs. 4, 7, 10, and 11. In Fig. 4 we observe that the scaled moduli change from the

regime of very small \tilde{k} values to the regime of very large \tilde{k} values when \tilde{k} changes by approximately four orders of magnitude. In Fig. 7 we observe that the rescaled moduli change from the regime of very small \tilde{m} to the regime of very large \tilde{m} when \tilde{m} changes by approximately 6 orders of magnitude. The different behavior in these two figures, namely, the fact that the change with \tilde{k} is more rapid than the change with \tilde{m} , is due to the different values of the two exponents T and T' which enter into the

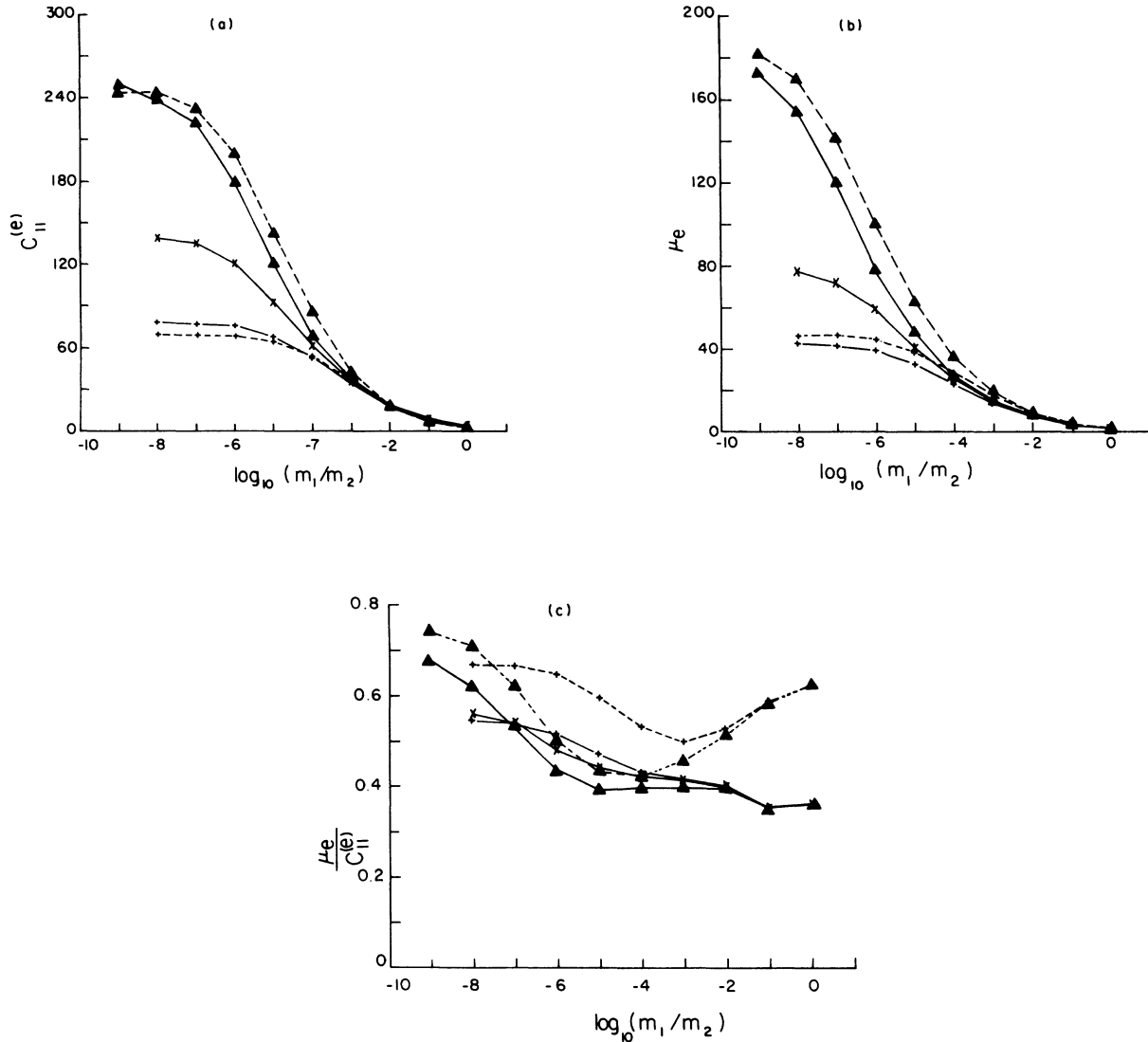


FIG. 9. (a) Values of $C_{11}^{(e)}$ plotted vs $\log_{10}(m_1/m_2)$. The points are the numerical simulation results for $L = 10$ (+), 20 (x), and 40 (▲). The lines are drawn through the points to guide the eye and to differentiate between the results with $k_1/m_1 = 15.82$ ($C_{11}^{(1)} = 2.8182$) (solid lines) and with $k_1/m_1 = 1.5$ ($C_{11}^{(1)} = 1.625$) (dashed lines). (b) Values of μ_e plotted vs $\log_{10}(m_1/m_2)$. The points are the numerical simulation results for $L = 10$ (+), 20 (x), and 40 (▲). The lines are drawn through the points to guide the eye and to differentiate between the results with $k_1/m_1 = 15.82$ ($C_{11}^{(1)} = 2.8182$) (solid lines) and with $k_1/m_1 = 1.5$ ($C_{11}^{(1)} = 1.625$) (dashed lines). (c) Values of $\mu_e/C_{11}^{(e)}$ plotted vs $\log_{10}(m_1/m_2)$. The points are the numerical simulation results for $L = 10$ (+), 20 (x), and 40 (▲). The lines are drawn through the points to guide the eye and to differentiate between the results with $k_1/m_1 = 15.82$ ($C_{11}^{(1)} = 2.8182$) (solid lines) and with $k_1/m_1 = 1.5$ ($C_{11}^{(1)} = 1.625$) (dashed lines).

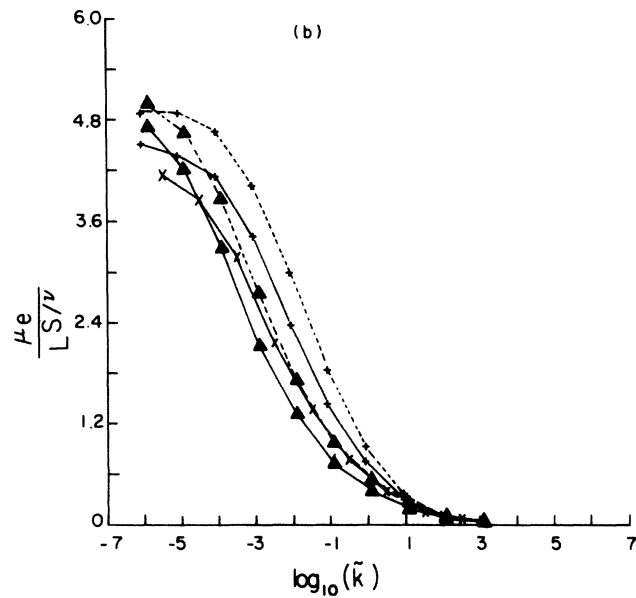
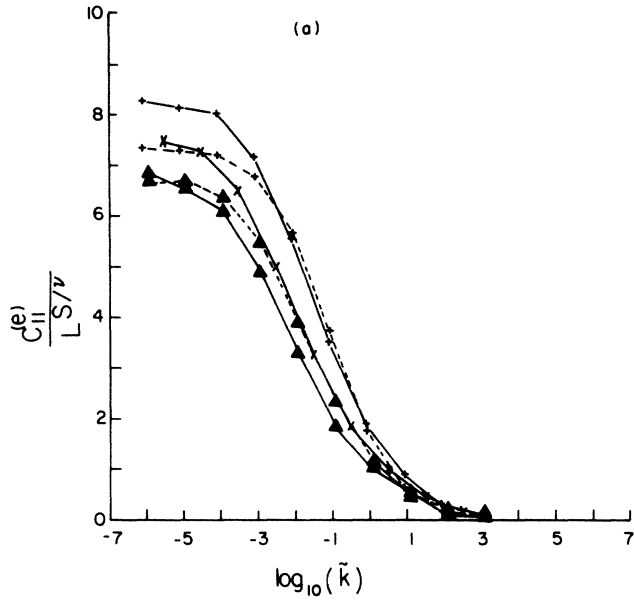


FIG. 10. (a) Values of $C_{11}^{(e)}/L^{S/\nu}$ plotted vs $\log_{10}(\tilde{k})$, with $T^* = 1.30$ and $S = 1.30$. The points are the numerical simulation results for $L = 10(+)$, $20(\times)$, and $40(\blacktriangle)$. The lines are drawn through the points to guide the eye and to differentiate between the results for $k_1/m_1 = 15.82$ ($C_{11}^{(1)} = 2.8182$) (solid lines) and for $k_1/m_1 = 1.5$ ($C_{11}^{(1)} = 1.625$) (dashed lines). (b) Values of $\mu_e/L^{S/\nu}$ plotted vs $\log_{10}(\tilde{k})$, with $T^* = 1.30$ and $S = 1.30$. The points are the numerical simulation results for $L = 10(+)$, $20(\times)$, and $40(\blacktriangle)$. The lines are drawn through the points to guide the eye and to differentiate between the results for $k_1/m_1 = 15.82$ ($C_{11}^{(1)} = 2.8182$) (solid lines) and for $k_1/m_1 = 1.5$ ($C_{11}^{(1)} = 1.625$) (dashed lines).

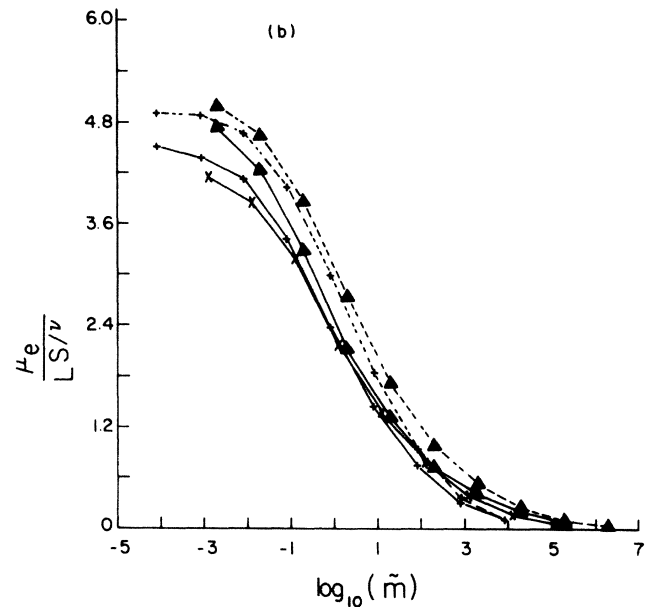
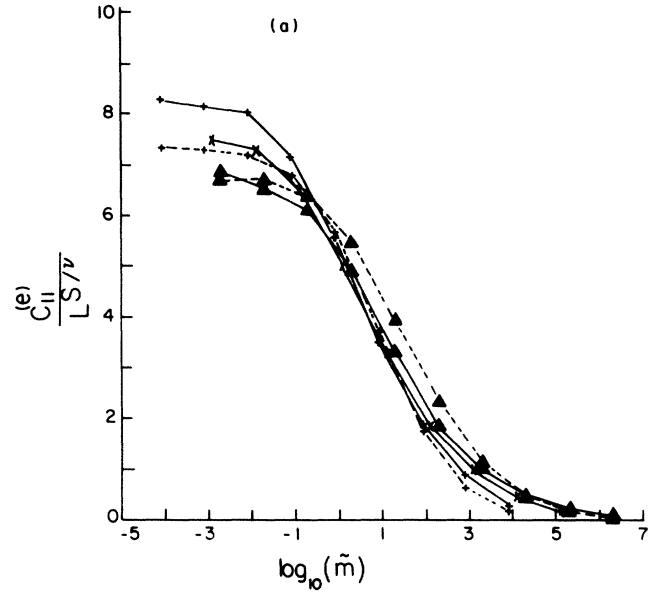


FIG. 11. (a) Values of $C_{11}^{(e)}/L^{S/\nu}$ plotted vs $\log_{10}(\tilde{m})$, with $T = 3.96$ and $S = 1.30$. The points are the numerical simulation results for $L = 10(+)$, $20(\times)$, and $40(\blacktriangle)$. The lines are drawn through the points to guide the eye and to differentiate between the results for $k_1/m_1 = 15.82$ ($C_{11}^{(1)} = 2.8182$) (solid lines) and for $k_1/m_1 = 1.5$ ($C_{11}^{(1)} = 1.625$) (dashed lines). (b) Values of $\mu_e/L^{S/\nu}$ plotted vs $\log_{10}(\tilde{m})$, with $T = 3.96$ and $S = 1.30$. The points are the numerical simulation results for $L = 10(+)$, $20(\times)$, and $40(\blacktriangle)$. The lines are drawn through the points to guide the eye and to differentiate between the results for $k_1/m_1 = 15.82$ ($C_{11}^{(1)} = 2.8182$) (solid lines) and for $k_1/m_1 = 1.5$ ($C_{11}^{(1)} = 1.625$) (dashed lines).

definitions of \bar{m} and \bar{k} , respectively. A similar difference in behavior, due to the same reason, is also apparent when we compare Figs. 10 and 11.

V. SUMMARY AND DISCUSSION

We investigated the scaling behavior of the bulk elastic moduli of a mixed normal-rigid elastic network at the

percolation threshold of the rigid component $p_2=p_c$. The bulk moduli were found to depend on two scaling variables, \bar{k} and \bar{m} , that depend in a different way on the finite width of a long (infinite) strip network at p_c . From finite-size scaling it then follows that the scaling variables for a network of infinite width away from p_c will depend in a different way on $\delta p \equiv p_2 - p_c$, namely

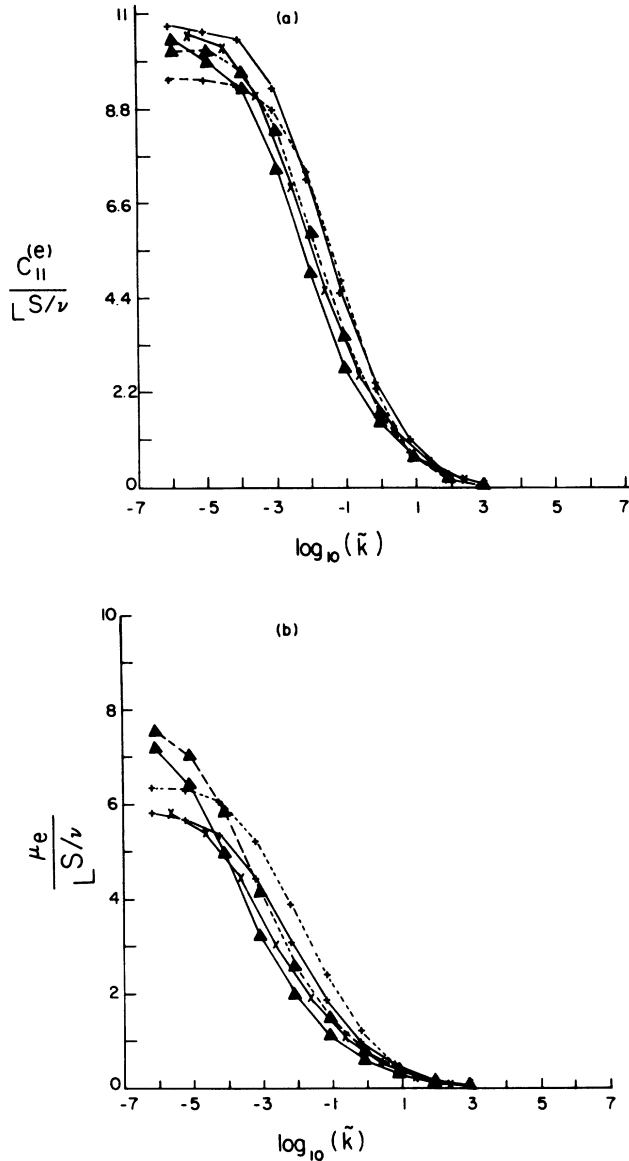


FIG. 12. (a) Values of $C_{11}^{(e)}/L^{S/\nu}$ plotted vs $\log_{10}(\bar{k})$, with $T'=1.1$ and $S=1.15$. The points are the numerical simulation results for $L=10$ (+), 20 (\times), and 40 (\blacktriangle). The lines are drawn through the points to guide the eye and to differentiate between the results for $k_1/m_1=15.82$ ($C_{11}^{(1)}=2.8182$) (solid lines) and for $k_1/m_1=1.5$ ($C_{11}^{(1)}=1.625$) (dashed lines). (b) Values of $\mu_e/L^{S/\nu}$ plotted vs $\log_{10}(\bar{k})$, with $T'=1.1$ and $S=1.15$. The points are the numerical simulation results for $L=10$ (+), 20 (\times), and 40 (\blacktriangle). The lines are drawn through the points to guide the eye and to differentiate between the results for $k_1/m_1=15.82$ ($C_{11}^{(1)}=2.8182$, $\mu^{(1)}=1.0$) (solid lines) and for $k_1/m_1=1.5$ ($C_{11}^{(1)}=1.625$, $\mu^{(1)}=1.0$) (dashed lines).

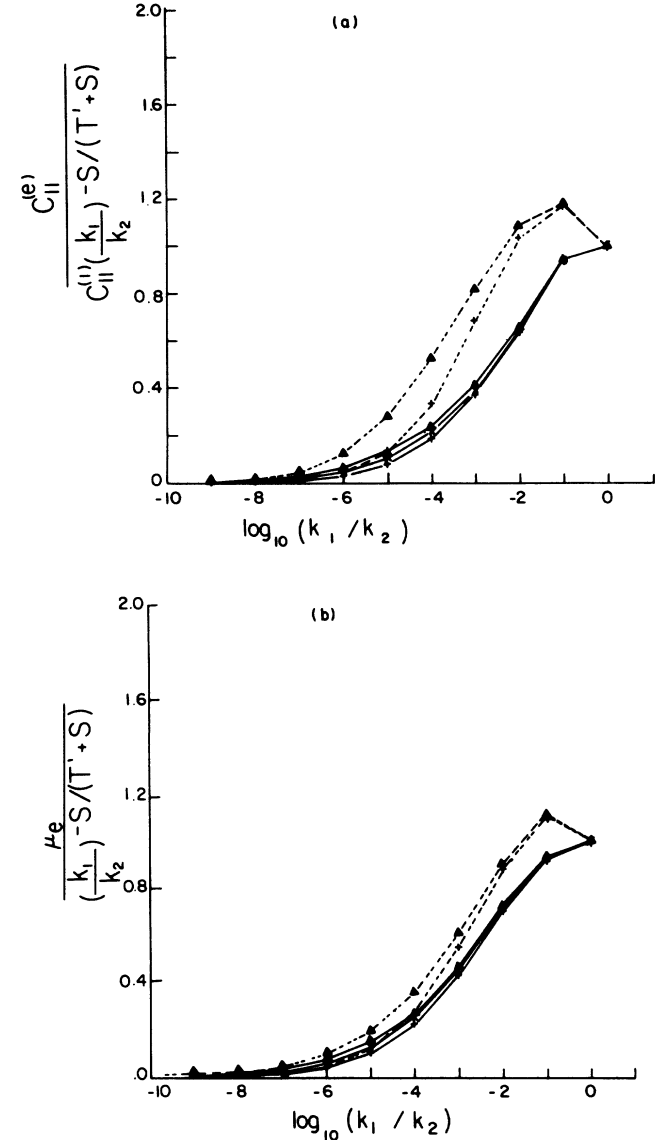


FIG. 13. (a) Values of $C_{11}^{(e)}/C_{11}^{(1)}(k_1/k_2)^{-S/(T'+S)}$ plotted vs $\log_{10}(k_1/k_2)$ with $T'=1.3$ and $S=1.3$. The points are the numerical simulation results for $L=10$ (+), 20 (\times), and 40 (\blacktriangle). The lines are drawn through the points to guide the eye and to differentiate between the results for $k_1/m_1=15.82$ ($C_{11}^{(1)}=2.8182$) (solid lines) and for $k_1/m_1=1.5$ ($C_{11}^{(1)}=1.625$) (dashed lines). (b) Values of $\mu_e/(C_{11}^{(1)}(k_1/k_2)^{-S/(T'+S)})$ plotted vs $\log_{10}(k_1/k_2)$ with $T'=1.3$ and $S=1.3$. The points are the numerical simulation results for $L=10$ (+), 20 (\times), and 40 (\blacktriangle). The lines are drawn through the points to guide the eye and to differentiate between the results for $k_1/m_1=15.82$ ($C_{11}^{(1)}=2.8182$, $\mu^{(1)}=1.0$) (solid lines) and for $k_1/m_1=1.5$ ($C_{11}^{(1)}=1.625$, $\mu^{(1)}=1.0$) (dashed lines).

$$\bar{k} = \frac{k_1/k_2}{|\delta p|^{T'+S}}, \quad (5.1a)$$

$$\bar{m} = \frac{m_1/m_2}{|\delta p|^{T'+S}}, \quad (5.1b)$$

where $T \simeq 3.96$ but $T' \simeq 1.3$, and $S \simeq 1.3$. We were able to give a tentative explanation for the appearance of the new exponent T' . We also found empirically that the bulk moduli seem to depend only on μ_1 —the shear modulus of the normal component—and are independent of the bulk modulus of that component κ_1 . At present we do not understand this phenomenon. It would also be nice if it could be tested in an experiment on a real composite material. Clearly, the elastic stiffness moduli of random composites near a rigidity or percolation threshold exhibit a rich variety of critical properties. Our investigation, which was based on numerical simulations of 2D random elastic networks, has demonstrated this quite vividly. It has also demonstrated the need for more extensive simulations, as well as the need for a better understanding of the basic physics that lies at the root of some of the empirical observations.

ACKNOWLEDGMENTS

This research was supported in part by a grant from the Israel Academy of Sciences and Humanities, by a grant from the Israel National Center for Absorption in Science, and by U.S. National Science Foundation (NSF) Grant No. DMR-84-14257.

APPENDIX

Here we describe some details of the transfer-matrix method used to simulate long 2D elastic strip networks. In Fig. 1(b) we show all ten sites whose displacements must be known in order to calculate the total internal force which acts upon the site at the center (marked 0). Using an obvious notation for the various bond-stretching and angle-bending force constants that appear in this figure, and likewise for the components of the site displacements, the two components of the force at the central site are given by [Fig. 1(b) should be consulted for an interpretation of the site indices in Eqs. (A1) and (A2)]

$$\begin{aligned} f_{0x} = & -k_{10}(u_{1x} - u_{0x}) - \left[\frac{k_{20}}{4} + \frac{3}{4}m_{102} + \frac{3}{2}m_{203} \right] (u_{2x} - u_{0x}) - \left(\frac{1}{4}k_{30} + \frac{3}{4}m_{103} + \frac{3}{2}m_{203} \right) (u_{3x} - u_{0x}) \\ & + \frac{\sqrt{3}}{2}(m_{103} - m_{102})(u_{1y} - u_{0y}) + \frac{\sqrt{3}}{4}(k_{20} - m_{102} - 2m_{203})(u_{2y} - u_{0y}) \\ & - \frac{\sqrt{3}}{4}(k_{30} - m_{103} - 2m_{203})(u_{3y} - u_{0y}) + \frac{3}{4}(m_{720} + m_{620})(u_{0x} - u_{2x}) + \frac{3}{4}m_{620}(u_{6x} - u_{2x}) \\ & + \frac{\sqrt{3}}{2}m_{720}(u_{7y} - u_{2y}) + \frac{\sqrt{3}}{4}(m_{720} + m_{620})(u_{0y} - u_{2y}) - \frac{\sqrt{3}}{4}m_{620}(u_{6y} - u_{2y}) + \frac{3}{4}m_{930}(u_{9x} - u_{3x}) \\ & + \frac{3}{4}(m_{830} + m_{930})(u_{0x} - u_{3x}) - \frac{\sqrt{3}}{2}m_{830}(u_{8y} - u_{3y}) + \frac{\sqrt{3}}{4}m_{930}(u_{9y} - u_{3y}) \\ & - \frac{\sqrt{3}}{4}(m_{830} + m_{930})(u_{0y} - u_{3y}), \end{aligned} \quad (A1)$$

$$\begin{aligned} f_{0y} = & \frac{\sqrt{3}}{4}(k_{20} - 3m_{102})(u_{2x} - u_{0x}) - \frac{\sqrt{3}}{4}(k_{30} - 3m_{103})(u_{3x} - u_{0x}) - \frac{2}{3}(m_{102} + m_{103})(u_{1y} - u_{0y}) \\ & - \frac{3}{4}(k_{20} + m_{102})(u_{2y} - u_{0y}) - \frac{3}{4}(k_{30} + m_{103})(u_{3y} - u_{0y}) + \frac{\sqrt{3}}{2}m_{410}(u_{4x} - u_{1x}) \\ & - \frac{\sqrt{3}}{2}m_{510}(u_{5x} - u_{1x}) + (m_{410} + m_{510})(u_{0y} - u_{1y}) + \frac{1}{2}m_{410}(u_{4y} - u_{1y}) + \frac{1}{2}m_{510}(u_{5y} - u_{1y}) \\ & + \frac{\sqrt{3}}{4}(m_{620} + m_{720})(u_{0x} - u_{2x}) + \frac{\sqrt{3}}{4}m_{620}(u_{6x} - u_{2x}) + \frac{1}{2}m_{720}(u_{7y} - u_{2y}) \\ & + \frac{1}{4}(m_{720} + m_{620})(u_{0y} - u_{2y}) - \frac{1}{4}m_{620}(u_{6y} - u_{2y}) - \frac{\sqrt{3}}{4}m_{930}(u_{9x} - u_{3x}) \\ & - \frac{\sqrt{3}}{4}(m_{830} + m_{930})(u_{0x} - u_{3x}) + \frac{1}{2}m_{830}(u_{8y} - u_{3y}) - \frac{1}{4}m_{930}(u_{9y} - u_{3y}) + \frac{1}{4}(m_{830} + m_{930})(u_{0y} - u_{3y}). \end{aligned} \quad (A2)$$

The procedure by which new bonds are added at the end of the strip is illustrated in Fig. 1(a). At each stage a triplet of new bonds is added—in Fig. 1(a), these are the bonds 14, 24, and 34. This involves adding three new stretching force constants k_{14} , k_{24} , k_{34} and six new bending force constants m_{415} , m_{417} , m_{426} , m_{243} , m_{142} , m_{143} , and two new sites at which external forces and displacements may be applied, namely, 4 and 3. At the same time the existing sites 5 and 1 may be dropped, since we are now able to calculate all the internal forces acting at those sites. We now demonstrate this first in the case of sites 5 and 4: From Eqs. (A1) and (A2) we find that when only the bending force constant m_{415} is added, the force components acting at the new site 4 are [Fig. 1(a) should be consulted for an interpretation of the site indices in Eqs. (A3)–(A12)]

$$\begin{aligned} F_{4x} &= 0, \\ F_{4y} &= m_{415} \left[-\frac{\sqrt{3}}{2}(u_{5x} - u_{1x}) + (u_{4y} - u_{1y}) \right. \\ &\quad \left. + \frac{1}{2}(u_{5y} - u_{1y}) \right]. \end{aligned} \quad (\text{A3})$$

At some of the other sites, additional forces act, given by

$$\begin{aligned} F_{5x} &= -\frac{\sqrt{3}}{2}F_{4y}, \quad F_{5y} = \frac{1}{2}F_{4y}, \\ F_{1x} &= \frac{\sqrt{3}}{2}F_{4y}, \quad F_{1y} = -\frac{3}{2}F_{4y}. \end{aligned} \quad (\text{A4})$$

We solve the second equation of (A3) for u_{4y}

$$u_{4y} = \frac{F_{4y}}{m_{415}} + \frac{3}{2}u_{1y} + \frac{\sqrt{3}}{2}u_{5x} - \frac{1}{2}u_{5y} - \frac{\sqrt{3}}{2}u_{1x}, \quad (\text{A5})$$

and we now substitute for the u_i 's on the rhs by their expressions in terms of the *new* external forces f'_i . The new external forces are the same as the old ones f_i except for those acting at sites 4, 1, and 5:

$$\begin{aligned} \mathbf{f}'_4 &= \mathbf{F}_4, \\ \mathbf{f}'_1 &= \mathbf{f}_1 + \mathbf{F}_1, \\ \mathbf{f}'_5 &= \mathbf{f}_5 + \mathbf{F}_5 = \mathbf{0}, \end{aligned} \quad (\text{A6})$$

where we have put $\mathbf{f}'_5 = \mathbf{0}$ since we have now included all the internal forces acting at 5. Therefore we can write, e.g.,

$$u_{1y} = \sum_{i (\neq 4)} B_{1y,i} f'_i = \sum_{i (\neq 4,5)} B_{1y,i} f'_i - B_{1y,1x} F_{1x} - B_{1y,1y} F_{1y} - B_{1y,5x} F_{5x} - B_{1y,5y} F_{5y}. \quad (\text{A7})$$

When this and similar expressions are substituted in (A5) we get, using (A4) and (A6) and collecting terms, and using the fact that $B_{ij} = B_{ji}$

$$\begin{aligned} u_{4y} &= \sum_{i (\neq 4,5)} \left[\frac{3}{2}B_{1y,i} - \frac{1}{2}B_{5y,i} + \frac{\sqrt{3}}{2}(B_{5x,i} - B_{1x,i}) \right] f'_i \\ &\quad + f'_{4y} \left[\frac{1}{m_{415}} + \frac{3}{4}B_{5x,5x} + \frac{1}{4}B_{5y,5y} + \frac{3}{4}B_{1x,1x} + \frac{9}{4}B_{1y,1y} - \frac{\sqrt{3}}{2}B_{5y,5x} \right. \\ &\quad \left. + \frac{3\sqrt{3}}{2}B_{1y,5x} - \frac{3}{2}B_{1x,5x} - \frac{3}{2}B_{1y,5y} + \frac{\sqrt{3}}{2}B_{1x,5y} - \frac{3\sqrt{3}}{2}B_{1y,1x} \right] \\ &\equiv \sum_i B'_{4y,i} f'_i. \end{aligned} \quad (\text{A8})$$

Thus we have calculated the elements $B'_{4y,i}$ of the new compliance matrix. The other elements may now be easily calculated too. In the new B matrix the site 5 has been replaced by the site 4. A similar procedure is followed when each one of the new force constants is added. We note that no difficulty is encountered in using (A8) even when $m_{415} = \infty$. That is why this algorithm can be used even when one component is infinitely stiff ($m = k = \infty$).

Next we added the force constant m_{417} , and this produces the following additional forces at sites 7,4,1:

$$\begin{aligned} F_{7x} &= m_{417} \left[\frac{3}{4}(u_{7x} - u_{1x}) \right. \\ &\quad \left. + \frac{\sqrt{3}}{2}(u_{4y} - u_{1y}) + \frac{\sqrt{3}}{4}(u_{7y} - u_{1y}) \right], \\ F_{7y} &= \frac{1}{\sqrt{3}}F_{7x}, \quad F_{4x} = 0, \\ F_{4y} &= \frac{2}{\sqrt{3}}F_{7x}, \quad F_{1x} = -F_{7x}, \quad F_{1y} = -\sqrt{3}F_{7x}. \end{aligned} \quad (\text{A9})$$

In the first of these equations we expand each u_i in terms of the new forces f'_i and the additional forces. Since the additional forces are all proportional to F_{7x} , we get an equation that can be solved to give F_{7x} in terms of the f'_i

$$DF_{7x} = \frac{\sqrt{3}}{2} \sum_i Q_i f'_i, \quad (\text{A10})$$

where

$$D = \frac{1}{m_{417}} + \frac{3}{4}B_{7x,7x} + \frac{1}{4}B_{7y,7y} + B_{4y,4y} + \frac{3}{4}B_{1x,1x} + \frac{9}{4}B_{1y,1y} - \frac{3}{2}B_{1x,7x} + \sqrt{3}B_{4y,7x} + \frac{\sqrt{3}}{2}B_{7y,7x} - \frac{3\sqrt{3}}{2}B_{1y,7x} - \frac{\sqrt{3}}{2}B_{1x,7y} + B_{4y,7y} - \frac{3}{2}B_{1y,7y} - \sqrt{3}B_{1x,4y} - 3B_{1y,4y} + \frac{3\sqrt{3}}{2}B_{1y,1x}, \quad (\text{A11})$$

$$Q_i = \frac{\sqrt{3}}{2}(B_{7x,i} - B_{1x,i}) + B_{4y,i} + \frac{1}{2}B_{7y,i} - \frac{3}{2}B_{1y,i}. \quad (\text{A12})$$

As long as $D \neq 0$, this can now be used to express all the additional internal forces F_i in terms of the new external forces f'_i and thus to translate the B matrix into its new form, namely

$$B'_{ij} = B_{ij} - \frac{Q_i Q_j}{D}. \quad (\text{A13})$$

When the force constants are all finite (and, of course, positive), B_{ij} is a symmetric positive definite matrix. These properties follow from the principle of reciprocity and from the fact that the elastic energy

$$\frac{1}{2} \sum_i f_i B_{ij} f_j, \quad (\text{A14})$$

is a positive definite quadratic form. The quantity D must also be positive. The fact that the linear combination of B_{ij} elements appearing in D is positive can be shown to arise from the positivity of the B matrix. However, when the force constants k_2, m_2 , of the rigid component tend to infinity, some eigenvalues of the B matrix, as well as some of the Q_i , may tend to zero. This occurs when different sites of the B matrix belong to the same finite rigid cluster: In that case it is possible to apply a set of nonzero forces f_i at those sites such that no forces will be transmitted outside that cluster, so that both inside and outside the cluster all the displacements vanish. It may even happen that D itself tends to zero, but in that case it follows from (A10) that *all* the Q_i must tend to zero. That is what saves (A13) from blowing up. Indeed, in those simulations where $k_2 = m_2 = \infty$, a considerable speeding up of the computations was achieved by skipping over the computing step described by (A13) whenever $D = 0$. The situation and considerations described here are entirely analogous to the situation and considerations in conducting networks, as discussed by Refs. 20 and 21. The equations and methods described in this Appendix were already used in previous simulations of rigid-normal networks^{13,14} and before that, with appropriate alterations, in simulations of normal-empty networks.^{5,12} In all of these simulations the most time consuming steps are of the form (A13), where all the elements of the compliance matrix must be revised. This type of step is also ideally

suited for taking advantage of the special characteristics of vector computers, and huge factors of speed up may be achieved, as noted by Refs. 21 and 12. Adding the other seven force constants to complete the new triplet of bonds is done by a straightforward extension of what we have described here—we omit the details because they become rather tedious.

At the end of the strip, a column of infinitely rigid-bond triplets is added, which is equivalent to the physical attachment of a rigid bar. The periodic boundary conditions at the long edges make the network effectively infinite in the x direction but with a finite period L_x , and finite but very large (of length $L_y \gg L_x$) in the y direction. The finite size that will appear in scaling expressions is the period L_x . The choice of initial conditions for the compliance matrix, namely $B_{ij} = 0$ at the beginning of the strip, is tantamount to attaching all the sites at the left-hand side to another, fixed rigid bar. Both bars make an angle θ with the y axis that is given by [see Fig. 1(c)]

$$\theta = \cot^{-1} \left[\frac{1}{\sqrt{3}} \left[1 + \frac{2}{L_x} \right] \right] = \frac{\pi}{3} - \frac{\sqrt{3}}{2L_x} + O(1/L_x^2). \quad (\text{A15})$$

This is not only slightly smaller than 60° , but depends on the strip width L_x and tends to 60° as $L_x \rightarrow \infty$. This is due to the special way in which the periodicity in the x direction was implemented [see Fig. 1(a)]. We could have made $\theta = 60^\circ$ independent of L_x by revising this implementation. This would have required rewriting a rather complicated computer program. However, we show below that it is easy to take the exact value of θ into account when calculating the bulk moduli for any L_x , and therefore we considered such a revision to be unnecessary.

In order to calculate, e.g., the bulk modulus $C_{11}^{(e)}$, we must apply a normal stress to the right-hand bar and figure out what is the normal uniaxial strain. This requires us to apply nonzero force components along both the x and y axes, in accordance with the value of the an-

gle θ . In order to calculate the bulk shear modulus μ_e , we must apply a force in parallel with the rigid bar and figure out the resulting parallel displacement. Again the value of θ must be used to take the right proportion of x

and y components. All of these procedures were checked out on a homogeneous version of the network, where all the bonds and angles had the same finite force constants, and where the results could be compared with Eqs. (2.1).

*Permanent address.

¹S. Feng and P. N. Sen, *Phys. Rev. Lett.* **52**, 216 (1984).

²Y. Kantor and I. Webman, *Phys. Rev. Lett.* **52**, 1891 (1984).

³D. J. Bergman and Y. Kantor, *Phys. Rev. Lett.* **53**, 511 (1984); see also D. J. Bergman, in *Proceedings of the Workshop on Physics of Disordered Systems*, Santa Barbara, 1983 (unpublished).

⁴L. Benguigui, *Phys. Rev. Lett.* **53**, 2028 (1984).

⁵D. J. Bergman, *Phys. Rev. B* **31**, 1696 (1985).

⁶S. Feng, M. F. Thorpe, and E. Garboczi, *Phys. Rev. B* **31**, 276 (1985).

⁷L. M. Schwartz, S. Feng, M. F. Thorpe, and P. N. Sen, *Phys. Rev. B* **32**, 4607 (1985).

⁸D. Deptuck, J. P. Harrison, and P. Zawadzki, *Phys. Rev. Lett.* **54**, 913 (1985).

⁹Y. Kantor, *J. Phys. A* **17**, L843 (1984).

¹⁰S. Feng and M. Sahimi, *Phys. Rev. B* **31**, 1671 (1985).

¹¹S. Feng, P. N. Sen, B. I. Halperin, and C. J. Lobb, *Phys. Rev. B* **30**, 5386 (1984).

¹²J. G. Zabolitzky, D. J. Bergman, and D. Stauffer, *J. Stat. Phys.* **44**, 211 (1986).

¹³D. J. Bergman, *Phys. Rev. B* **33**, 2013 (1986).

¹⁴D. J. Bergman and E. Duering, *Phys. Rev. B* **34**, 8199 (1986).

¹⁵J. P. Straley, *Phys. Rev. B* **15**, 5733 (1977).

¹⁶Y. Imry and D. J. Bergman, *Phys. Rev. A* **3**, 1416 (1971).

¹⁷M. E. Fisher, in *Critical Phenomena*, Proceedings of the International School of Physics "Enrico Fermi", Course No. LI, Varenna, 1971, edited by M. S. Green (Academic, New York, 1972), pp. 1–99.

¹⁸C. J. Lobb and D. J. Frank, *J. Phys. C* **12**, L827 (1979).

¹⁹V. K. S. Shante and S. Kirkpatrick, *Adv. Phys.* **20**, 325 (1971).

²⁰B. Derrida and J. Vannimenus, *J. Phys. A* **15**, L557 (1982).

²¹H. J. Herrmann, B. Derrida, and J. Vannimenus, *Phys. Rev. B* **30**, 4080 (1984).